The Dispersal of Dense Water Formed in an Idealized Coastal Polynya on a Shallow Sloping Shelf

WEIFENG G. ZHANG

*Applied Ocean Physics and Engineering Department, Woods Hole Oceanographic Institution,
Woods Hole, Massachusetts*

CLAUDIA CENEDESE

*Physical Oceanography Department, Woods Hole Oceanographic Institution,
Woods Hole, Massachusetts*

ABSTRACT

This study examines the dispersal of dense water formed in an idealized coastal polynya on a sloping shelf in the absence of ambient circulation and stratification. Both numerical and laboratory experiments reveal two separate bottom pathways for the dense water: an offshore plume moving downslope into deeper ambient water and a coastal current flowing in the direction of Kelvin wave propagation. Scaling analysis shows that the velocity of the offshore plume is proportional not only to the reduced gravity, bottom slope, and inverse of the Coriolis parameter, but also to the ratio of the dense water depth to total water depth. The dense water coastal current is generated by the along-shelf baroclinic pressure gradient. Its dynamics can be separated into two stages: (i) near the source region, where viscous terms are negligible, its speed is proportional to the reduced gravity wave speed and (ii) in the far field, where bottom drag becomes important and balances the pressure gradient, the velocity is proportional to $H_c[g'/(LC_d)]^{1/2}$ in which H_c is the water depth at the coast, g' the reduced gravity, C_d the quadratic bottom drag coefficient, and L the along-shelf span of the baroclinic pressure gradient. The velocity scalings are verified using numerical and laboratory sensitivity experiments. The numerical simulations suggest that only 3%–23% of the dense water enters the coastal pathway, and the percentage depends highly on the ratio of the velocities of the offshore and coastal plumes. This makes the velocity ratio potentially useful for observational studies to assess the amount of dense water formed in coastal polynyas.

1. Introduction

Coastal polynyas are an important component of the Arctic climate system as they enhance the fluxes of momentum, heat, moisture, and biogeochemical tracers across the air–sea interface and affect local biological communities (Morales Maqueda et al. 2004). Coastal polynyas can also affect the Arctic Ocean circulation in the deep basins through the supply of dense waters to the Arctic halocline that separates the cold, fresh surface mixed layer from the subsurface warm Atlantic water and, therefore, shields sea ice from the heat stored at depth (Aagaard et al. 1981). Owing to the constant heat loss to the atmosphere, ice is continually generated in the polynya region and pushed away by offshore winds. The associated brine rejection forms dense water, which is reported to be a potentially major source of Arctic halocline water (Cavalieri and Martin 1994; Winsor and Björk 2000).

To supply the Arctic halocline in the deep basins, dense water that forms in coastal polynyas must travel across the shallow continental shelves, from the source regions to the shelf edges, to reach the open ocean. The transport and dispersal of the dense waters on the sloping continental shelves and the mechanisms responsible for the dispersal are therefore worth investigating. Few direct observations of dense water dispersal are available due to the difficulties of taking measurements in the ice-covered winter season, and most prior studies on the subject are either analytical or numerical (Chapman

Corresponding author address: Weifeng G. Zhang, Applied Ocean Physics and Engineering Department, Woods Hole Oceanographic Institution, 266 Woods Hole Road, Woods Hole, MA 02543.
E-mail: wzhang@whoi.edu

1999, 2000; Chapman and Gawarkiewicz 1995, 1997; Gawarkiewicz 2000; Gawarkiewicz and Chapman 1995; Wilchinsky and Feltham 2008; Winsor and Chapman 2002). These studies have shown that (i) much of the offshore dispersal of the dense water generated in a coastal polynya occurs in the form of eddies, (ii) irregular topography on the shelf (e.g., canyons) tends to facilitate the dispersal, and (iii) ambient currents and meteorological forcing can also influence the offshore transport of the dense water. In this work, we will focus on the dynamics of two separate dispersal pathways of the dense water formed in an idealized coastal polynya on a shallow shelf.

Dispersal of the dense water generated in a coastal polynya on a sloping bottom differs from that of the dense water injected horizontally into the ocean from a coast [e.g., a hyperpycnal river outflow (Chen et al. 2013)] in that the former has no initial horizontal momentum when it first enters the ocean and can therefore remain in the volume underneath the polynya for a relatively long period of time. Over that period, the dynamical evolution of the dense water is not only controlled by the gravitational force down the sloping bottom, the Coriolis force, and the horizontal baroclinic pressure gradient, but also constrained by the presence of the coastal boundary (the coastline or edge of landfast ice). Our numerical and laboratory experiments show two separate bottom pathways of dense water dispersal: (i) a relatively well-known offshore pathway in which dense water moves initially down the slope and then turns to the right (looking downslope in the Northern Hemisphere) and (ii) a coastal pathway in the form of a dense water bottom coastal current flowing in the direction of Kelvin wave propagation.

The offshore pathway (hereafter referred to as offshore plume) has been investigated in numerous theoretical, numerical, and laboratory studies focusing on the dynamics of dense water overflows (e.g., Cenedese et al. 2004; Etling et al. 2000; Jiang and Garwood 1996; Lane-Serff and Baines 1998; Price and Baringer 1994; Wobus et al. 2011). The dense water coastal current on the bottom (hereafter referred to as the bottom coastal current) has been examined by Wilchinsky and Feltham (2008) in an idealized Antarctic polynya on a deep shelf (400 m) and also appeared in figures of other numerical [Fig. 2 in Chapman (2000)] and laboratory [Fig. 5 in Etling et al. (2000)] studies. The bottom coastal current bears some similarity to a surface buoyant gravity current flowing along the coast (e.g., Griffiths and Hopfinger 1983; Hacker and Linden 2002; Lentz and Helfrich 2002; Stern et al. 1982; Yankovsky and Chapman 1997) where the main dynamical balance is between the nonlinear terms and the along-shelf baroclinic pressure

gradient. However, as will be shown in this study, bottom friction can exert a profound influence on the bottom coastal current after an initial period of time.

The main goal of this study is to provide a dynamical description of both dense water dispersal pathways formed in a coastal polynya on a shallow sloping shelf. In particular, we investigate the dependence of the velocities of the offshore plume and bottom coastal currents on external parameters (i.e., bottom slope, buoyancy forcing, bottom friction, Coriolis parameter, and water depth at the coast). Velocity scalings are derived from momentum balances in the pathways and compared with results from the numerical and laboratory sensitivity experiments. Here, we neglect the influences of ambient currents and stratification, irregular topography, and external forces on the dense water dispersal and simplify the ice edge as a coastal wall. Although our analysis focuses on the dispersal pattern of dense water as it forms in shallow coastal polynyas, the results obtained are relevant for the dispersal of dense water released into an ocean over a sloping bottom near a coastline or steep topography, provided the assumptions made in our analysis are valid.

2. Methods

a. Numerical model setup

The hydrostatic Regional Ocean Modeling System (ROMS) (Haidvogel et al. 2008; Shchepetkin and McWilliams 2008) is used to simulate the dense water formation and dispersal. The coordinates are defined as follows: positive x is directed along shelf (east) with the coast on the right, positive y points offshore (north), and positive z points upward with $z = 0$ defined at the free surface. The model has a rectangular domain (Fig. 1a) with edge lengths of $L_x = 300$ km and $L_y = 150$ km and a uniform horizontal resolution of 500 m. The bathymetry deepens toward the north with a constant slope $\alpha = \tan\beta$, where β is the angle between the slope and the horizontal, and the bathymetry is uniform in the east–west direction (i.e., along shelf). The model has 60 vertical layers with high vertical resolution toward the bottom. The northern and southern boundaries are closed. All variables on the western boundary are fixed at their initial values. Chapman (1985), Flather (1976), and Orlanski-type radiation (Orlanski 1976) conditions are used on the eastern boundary for surface elevation, barotropic velocity, and baroclinic variables, respectively. A uniform Coriolis parameter f is used for the entire domain. A quadratic bottom friction parameterization with drag coefficient C_d is implemented. A generic length-scale turbulence closure k–kl scheme
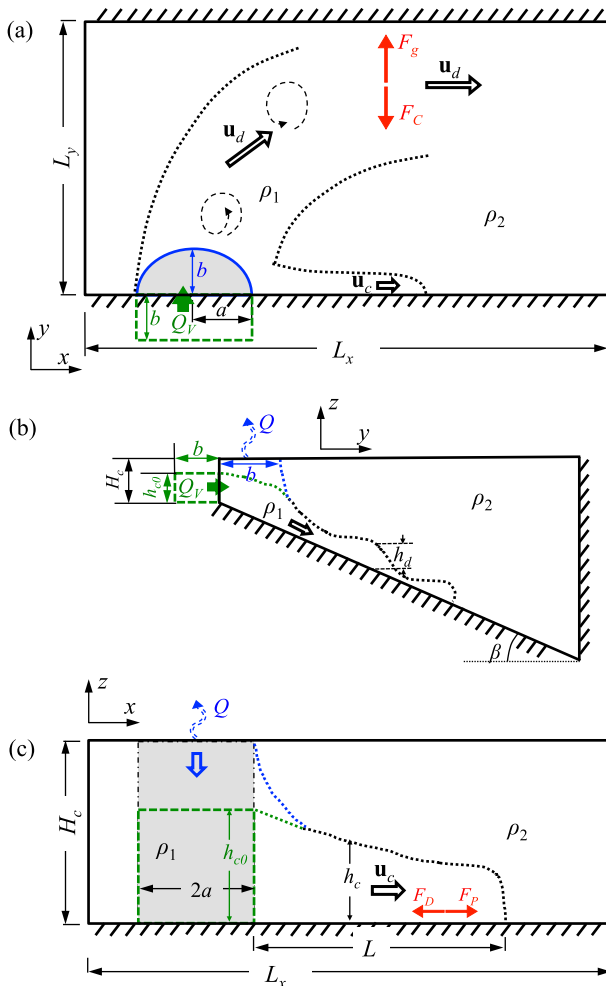
FIG. 1. (a) Plan, (b) side, and (c) front view of the numerical and laboratory domains. Sketches of the dense water dispersal pathways and dominant force balances [red arrows in (a) and (c)]. The blue and green symbols are for the numerical and laboratory experiments, respectively, and black symbols are for both.

(Warner et al. 2005) is used to parameterize vertical mixing associated with subgrid-scale processes, including unresolved nonhydrostatic processes. We will discuss the implication of the hydrostatic approximation in section 3c.

To simplify the computation, the temperature equation of the model is neglected and only the salinity equation is considered. A linear equation of state with a saline contraction coefficient of $7.9 \times 10^{-4} \, \mathrm{psu}^{-1}$ is used. The initial density is uniform in the entire model domain. Brine rejection in the polynya is simulated with a steady and uniform salt flux into the ocean (equivalent to a negative surface buoyancy flux Q) over a prescribed half-elliptic area next to the southern coast with semimajor and semiminor axes of $a = 25 \, \mathrm{km}$ and $b = 10 \, \mathrm{km}$, respectively (gray area in Fig. 1a). There is no surface

salt exchange outside of the polynya area, and no surface momentum exchange is applied anywhere in the domain. Previous studies of coastal polynyas often used a forcing decay region to represent the variation of polynya size on time scales smaller than that of ocean responses (Chapman 1999). In the present study, to avoid ambiguities in calculations of the distances the dense plumes have traveled, we neglect the forcing decay region, as simulations with and without the decay region show almost no difference in the two-pathway pattern of the dense water dispersal away from the polynya after an initial period of adjustment.

Values of the key parameters in the control simulation are given in Table 1. For the sensitivity analysis, we conduct a series of simulations for each target parameter (α, Q, C_d, f, and the water depth at the coast, H_c). Within each series, only the value of the target parameter is altered (see Table 1 for the range of values), and the values of all other parameters are kept the same as in the control simulation. There are a total of 33 simulations, including the control simulation.

b. Laboratory setup

The laboratory experiments are conducted in a glass tank of depth 60 cm and length and width $L_x = L_y = 60 \, \mathrm{cm}$. The tank is mounted on a 1-m diameter rotating turntable with a vertical axis of rotation. A square tank is used to avoid optical distortion from side views associated with a circular tank. The bottom of the tank has a constant slope α. The tank is filled with freshwater of density ρ_1, which is initially in solid-body rotation. A reservoir of salted and dyed water of density $\rho_2 > \rho_1$ is placed on the rotating table and connected to a source on the sloping bottom, via a pump and a plastic tube.

The source is positioned on the left-hand side (looking downslope) of the shallowest part of the tank (Fig. 1a, green dashed rectangle) and consists of a plastic rectangular box with side lengths of $2a = 6.7 \, \mathrm{cm}$ and $b = 6 \, \mathrm{cm}$ and with the wall looking downslope, 0.5 cm in height, removed. The plastic tube from the pump is connected to an opening made on top of the source, and the dense water fills the entire source box and then exits on the downslope side. The dense source was designed to give no horizontal momentum to the dense water and to allow the accumulation of dense water near the source region as in a coastal polynya. The experimental apparatus is similar to that used in Cenedese and Adduce (2008) with the addition of a vertical wall positioned along shelf at the depth of the dense water source. The introduction of the vertical wall is dictated by the observation that in coastal polynyas dense water is generated near a vertical boundary, that is, the coastline or edge of land-fast ice. Although the mechanism of dense

TABLE 1. Parameters of the numerical model sensitivity experiments.

Parameter	Symbol	Unit	Control value	Min value	Max value	Range of Fr_d	Range of Ek_d	Range of Fr_c
Bottom slope	α	10^{-3}	1	0.25	3	$0.054 \sim 0.12$	$0.013 \sim 0.086$	$0.091 \sim 0.15$
Surface buoyancy flux	Q	$10^{-7}\,m^2\,s^{-3}$	4[a]	2	16	$0.055 \sim 0.14$	$0.025 \sim 0.13$	$0.11 \sim 0.20$
Quadratic bottom drag	C_d	10^{-3}	3	0.3	30	$0.068 \sim 0.095$	$0.0026 \sim 2.9$	$0.079 \sim 0.24$
Coriolis parameter	f	$10^{-4}\,s^{-1}$	1.3[b]	0.5	3	$0.059 \sim 0.10$	$0.0021 \sim 0.44$	$0.13 \sim 0.14$
Water depth at the coast	H_c	m	30[c]	10	50	$0.061 \sim 0.18$	$0.020 \sim 0.067$	$0.11 \sim 0.14$

[a] $Q = 4 \times 10^{-7}\,m^2\,s^{-3}$ is a typical surface buoyancy flux for coastal polynyas in the Chukchi Sea area (Winsor and Chapman 2002).
[b] $f = 1.3 \times 10^{-4}\,s^{-1}$ corresponds to the latitude of 63°N.
[c] $H_c = 30\,m$ is a typical water depth at the seaward land-fast ice edge off the north coast of Alaska in winter (Mahoney et al. 2007).

water generation is different than in a coastal polynya, the dense water source provides a more controllable setup in the laboratory.

A total of 22 experiments were conducted, including the control experiment which was repeated twice. After the ambient fluid is spun up, the experiment starts by turning on the pump. At the end of each experiment, the water in the tank is mixed and a new ambient density is measured for the next experiment using a DMA58 Anton Paar densitometer with an accuracy of $10^{-2}\,kg\,m^{-3}$. A video camera is mounted above the tank and fixed to the turntable so that measurements are obtained in the rotating frame. The dense current is made visible by dyeing the fluid with food coloring and is observed both from the top and the side. The depth of the ambient freshwater at the "coast," H_c, is kept constant at 0.10 m for every slope inclination. Depth H_c is always greater than the thickness of the dense water near the source, h_{c0}, which is measured by eye, with an error of approximately $\pm 5 \times 10^{-4}\,m$, looking at the side of the tank where a ruler, attached to the sidewall, is placed orthogonal to the sloping bottom. Values of the key parameters in the control experiment are given in Table 2. The sensitivity experiments for each of the target parameters (α, f, the reduced gravity g', and the dense water flow rate Q_V) are conducted by varying only the value of the target parameter, while keeping the other parameters the same as in the control experiment (Table 2). Here $g' = g\Delta\rho/\rho_0$, where g is the gravitational acceleration, $\Delta\rho$

is the density difference between the dense and ambient waters, and ρ_0 is the reference density.

Differences in the target parameter sets in the numerical and laboratory sensitivity experiments result mostly from the different methods used to supply the dense water. The constant dense water supply at the base of the "coastal wall" in the laboratory allows g' to be treated as an external control variable with the sensitivity analysis conducted directly against it. Because in the laboratory h_{c0} and the representative thickness of the bottom coastal current h_c (h_c is assumed to be $h_{c0}/2$; see section 3d) are independent of H_c, it is more relevant to investigate the sensitivity of the velocities of the dense currents to h_{c0} or h_c rather than H_c. The sensitivity analysis to h_c is carried out by varying Q_V, as h_c is not an external control variable in the laboratory but is directly affected by Q_V. Larger values of Q_V are observed to generate thicker dense currents, that is, larger values of h_c. In the numerical simulations, the prescribed surface buoyancy flux Q is an external control variable and, together with H_c, determines the value of g' (section 3b). Hence, sensitivities to both Q and H_c are sought in the numerical simulations. Another difference in the target parameters is the bottom drag coefficient C_d, which is a control variable in the numerical model, but not in the laboratory experiments. The bottom boundary layer is inherently present in the laboratory experiments, and we do not examine the sensitivity of the current velocities to bottom friction in that setting.

TABLE 2. Parameters of the laboratory sensitivity experiments.

Parameter	Symbol	Unit	Control value	Min value	Max value	Range of Fr_d	Range of Ek_d ($\times 10^{-3}$)	Range of Fr_c
Bottom slope	α	—	0.21	0.05	0.31	$0.039 \sim 0.090$	$0.12 \sim 0.26$	$0.18 \sim 0.27$
Reduced gravity	g'	$m\,s^{-2}$	0.012	0.001	0.051	$0.063 \sim 0.10$	$0.050 \sim 0.78$	$0.23 \sim 0.35$
Coriolis parameter	f	s^{-1}	4.0	2.0	4.0	$0.083 \sim 0.090$	$0.17 \sim 0.43$	$0.26 \sim 0.30$
Volume flux	Q_V	$10^{-6}\,m^3\,s^{-1}$	3.3	0.92	5.3	$0.049 \sim 0.11$	$0.11 \sim 0.62$	$0.10 \sim 0.33$
Water depth at the coast*	h_{c0}	m	0.05	0.025	0.099	—	—	—

* Depth h_{c0} is not an external control variable in the laboratory experiments, but closely related to Q_V. Its control value and range are provided here for reference.
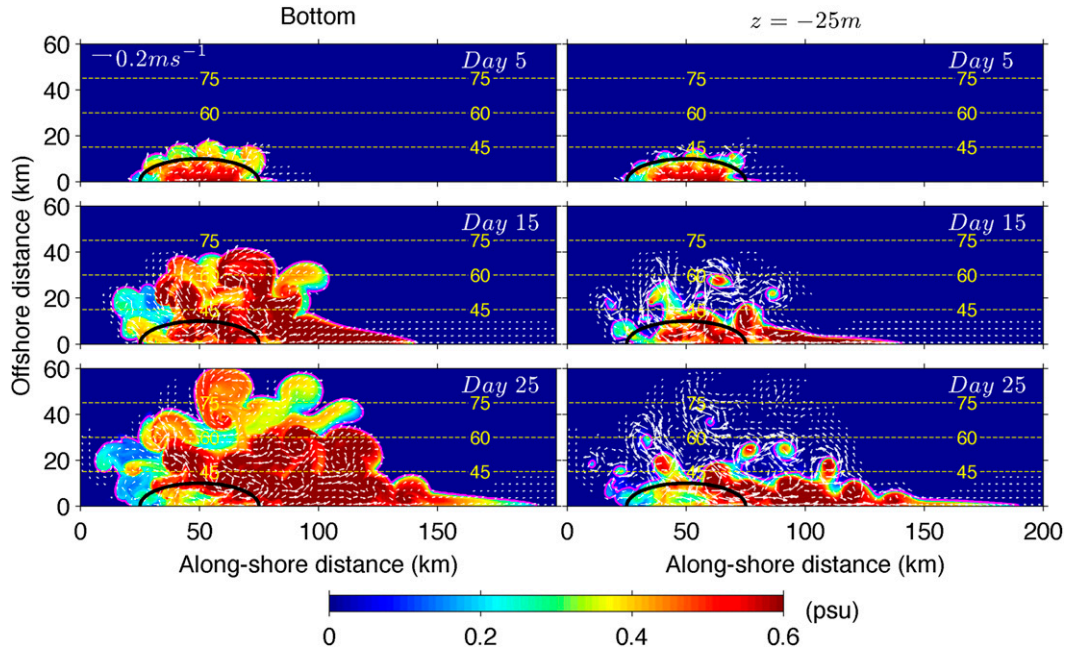
FIG. 2. Modeled (color) salinity anomaly and (white vectors) velocity vectors (left) near the bottom and (right) at 25 m below the surface at days (top) 5 (inertial period 9), (middle) 15 (inertial period 26), and (bottom) 25 (inertial period 44). Velocity vectors of speed less than $0.015\,\mathrm{m\,s}^{-1}$ are omitted for clarity. The velocity scale is shown at the top left. Black solid lines outline the polynya-forcing area, dashed yellow lines indicate isobath contours, and magenta solid lines are the salinity anomaly contour of 0.2 psu.

3. Results

a. General pattern

The numerical and laboratory experiments consistently show two separate pathways of the bottom dispersal of the dense water (Figs. 2 and 3, left columns): (i) in the offshore plume, the dense water flows initially downslope after approximately five and one inertial periods in the numerical and laboratory experiments, respectively, and then turns gradually to the right (looking downslope in the Northern Hemisphere); (ii) the other branch of the dense water, the bottom coastal current, travels on the bottom along the vertical wall in the direction of Kelvin wave propagation. The difference in the time taken by the dense water to first leave the forcing area in the numerical and laboratory experiments could be caused by the different methods of supplying the dense water. The dense water supply at the base of the "coastal wall" in the laboratory setup allows the dense water to undergo lateral transitions immediately after entering the "ocean," whereas in the numerical setup dense water must first mix through the entire water column gradually before reaching the bottom and spreading laterally.

The dynamical regime of the offshore plume can be characterized by the values of the Froude and Ekman numbers (Cenedese et al. 2004) defined respectively as

$$\mathrm{Fr}_d = \frac{|\mathbf{u}_d|}{\sqrt{g'h_d}} \qquad (1)$$

and

$$\mathrm{Ek}_d = \left(\frac{\delta}{h_d}\right)^2. \qquad (2)$$

Here $|\mathbf{u}_d|$ and h_d are the mean velocity and depth of the offshore plume, respectively (subscript d indicates properties of the offshore plume), and δ is the thickness of the bottom Ekman layer. In the laboratory settings, because the flows are laminar and kinematic viscosity is constant, $\nu = 10^{-6}\,\mathrm{m^2\,s^{-1}}$, δ can be estimated as $\delta^2 \approx 2\nu/f$, so (2) becomes

$$\mathrm{Ek}_d \approx \frac{2\nu}{fh_d^2}. \qquad (3)$$

In the laboratory control experiment (Figs. 3a–c) $|\mathbf{u}_d| \approx 0.002\,\mathrm{m\,s}^{-1}$, $g' \approx 0.01\,\mathrm{m\,s}^{-2}$, $h_d \approx h_{c0} \approx 0.05\,\mathrm{m}$, and $f = 4\,\mathrm{s}^{-1}$. Substituting these values into (1) and (3) gives $\mathrm{Fr}_d \approx 0.09$ and $\mathrm{Ek}_d \approx 2 \times 10^{-4}$, satisfying the condition of the eddy regime category ($\mathrm{Fr}_d < 1$ and $\mathrm{Ek}_d < 0.1$) suggested by Cenedese et al. (2004).

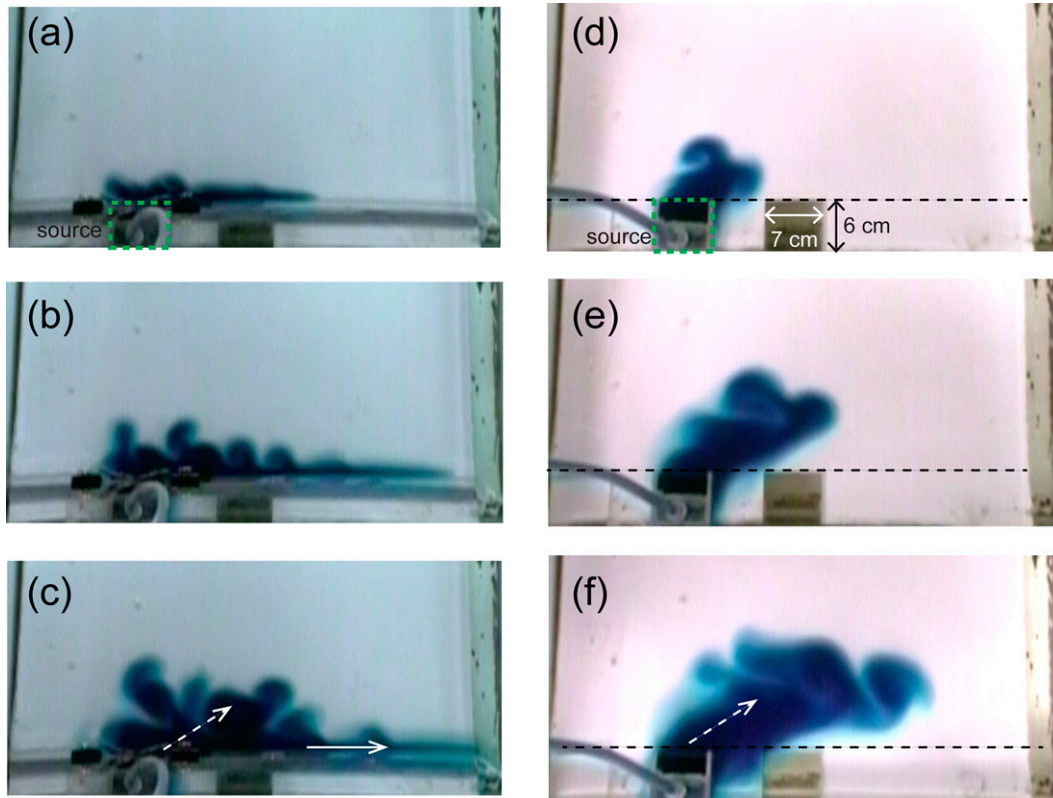In the numerical settings, ν in the turbulent bottom boundary layers (BBL) varies with depth, and the

FIG. 3. Time series of dense water (dyed blue) flowing down a slope in the (left) presence and (right) absence of a vertical "southern" wall: (a),(d) taken after $9T$, (b),(e) after $24T$, and (c),(f) after $44T$, where T is the rotation period. Black dashed lines in (d)–(f) outline the position of the vertical wall in (a)–(c); white dashed arrows indicate the downslope movement of the dense fluid, while the white solid arrow indicates the dense current traveling along the vertical wall in the direction of Kelvin wave propagation; and the green dashed box in (a) and (d) indicates the source box.

aforementioned method of estimating Ek_d cannot be applied. Here, we assume δ is equal to the thickness of the stably stratified BBL and therefore it satisfies the formula (Killworth and Edwards 1999; Zilitinkevich and Mironov 1996):

$$\left(\frac{\delta}{C_n u_*/f}\right)^2 + \frac{\delta}{C_i u_*/N_b} = 1, \qquad (4)$$

where u_* and N_b are the friction velocity and buoyancy frequency in the BBL, respectively, and C_n and C_i are constants with $C_n = 0.5$ and $C_i = 20$. Using a quadratic drag formula, u_* can be expressed as $u_* = \sqrt{\tau_b/\rho_0} \approx C_d^{1/2}|\mathbf{u}_d|$. Here, τ_b is the bottom stress, and we assume the near bottom velocity $|\mathbf{u}_b| \approx |\mathbf{u}_d|$. In the numerical control simulation (Fig. 2), $|\mathbf{u}_d| \approx 0.03\,\mathrm{m\,s^{-1}}$, $g' \approx 0.01\,\mathrm{m\,s^{-2}}$, $h_d \approx 10\,\mathrm{m}$, $N_b \approx 0.012\,\mathrm{s^{-1}}$, $f = 1.3 \times 10^{-4}\,\mathrm{s^{-1}}$, $C_d = 0.003$, and, according to (4), $\delta \approx 2\,\mathrm{m}$. Substituting these values into (1) and (2) gives $\mathrm{Fr}_d \approx 0.09$ and $\mathrm{Ek}_d \approx 0.04$, also satisfying the condition of the eddy regime category.

Consistent with Cenedese et al. (2004), the offshore transport of dense water in both numerical and laboratory experiments is primarily in the form of eddies (Figs. 2 and 3). In the numerical model, the dense water eddies have radii of about 10 km; above the dense water eddies, cyclonic vortices with similar radii (Fig. 2, right) are generated in the upper water column by conservation of potential vorticity (see below for more discussion). In the laboratory, the dense water eddies have a radius of approximately 0.03–0.04 m (Fig. 3c), and cyclonic velocities over them are also observed (not shown). This pattern of dense water offshore transport is very similar to that observed in a number of earlier studies (e.g., Chapman and Gawarkiewicz 1997; Etling et al. 2000).

The small Ek_d in both setups indicates that the BBL is much thinner than the descending dense water layer and the bottom friction is small in the momentum balance of the offshore plume. The baroclinic Rossby radius of deformation for the dense water $R_D = (g'h_d)^{1/2}/f$ is
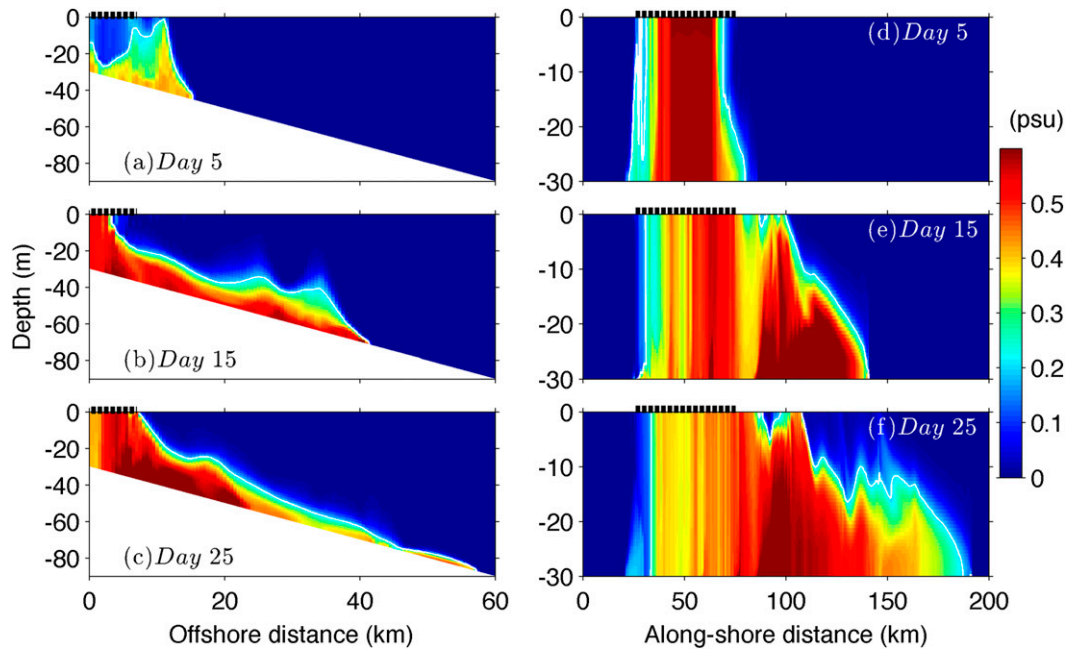
FIG. 4. Offshore and along-shelf sections of salinity anomaly at days (top) 5 (inertial period 9), (middle) 15 (inertial period 26), and (bottom) 25 (inertial period 44). The offshore section is taken at the along-shelf distance $x = 70$ km (see Fig. 2), and the along-shelf section is taken at the southern wall. Black dashed lines indicate the polynya-forcing region, and white solid lines are the salinity anomaly contour of 0.2 psu.

≈ 2 km and 5.5×10^{-3} m in the numerical and laboratory control experiments, respectively, and, since it is smaller than the width of the source in both setups, R_D is used to compute the Rossby number $\mathrm{Ro}_d = |\mathbf{u}_d|/(fR_D)$, which is equivalent to the Fr_d. In our study, $\mathrm{Ro}_d \ll 1$, indicating that nonlinear momentum advection is much smaller than the Coriolis force in the offshore plume. The radii of the dense eddies appear somewhat larger than R_D, suggesting that ageostrophic processes may be involved in shaping the eddies. The downslope gravitational force is likely the cause, as it could pull the dense water offshore from the dense eddy cores initially trapped under the upper-layer cyclonic vortices, and this process tends to widen the dense eddies. The formation of the eddies will be discussed in section 3b.

The bottom coastal current flows along the coast with meanders and eddies trailing behind, and some of the eddies flow downslope connecting the bottom coastal current to the offshore plume (Figs. 2 and 3). The width of the bottom coastal current decreases almost linearly from the point where the two pathways separate to its nose. The height of the dense water current also varies along the coast and decreases gradually from the separation point toward the nose (Figs. 4d–f). This wedge shape is similar to that of buoyant gravity currents moving along a vertical wall in a rotating fluid [Fig. 3 in Griffiths and Hopfinger (1983)]. Figures 4d–f show that

the length of the wedge in the numerical model increases with time, from about 10 km at day 5 to about 100 km at day 25.

For polynyas on a 400-m-deep shelf, the Wilchinsky and Feltham (2008) results suggest that the presence of a neighboring coastal wall is necessary for the formation of the bottom coastal current. To extend this to polynyas on a shallow shelf, we compare two pairs of experiments, one numerical and the other laboratory, with and without the southern coastal wall. The setup of the first simulation in the numerical pair is the same as that of the control simulation, except that now $H_c = 50$ m (Fig. 5, left); in the second simulation, the southern wall is moved to the south by 45 km while $\alpha = 0.001$ is preserved (Fig. 5, right). The laboratory pair consists of the laboratory control experiment (Fig. 3, left) and another experiment with the southern wall removed (Fig. 3, right). The buoyancy forcing or dense water source is the same in each experiment pair. Comparison of the dense water pathways in Figs. 3 and 5 confirms the role of the coastal wall in forming the bottom coastal current. In particular, without the vertical wall next to the buoyancy forcing region, the dense water tends to first accumulate around the forcing area, then to move gradually downslope, and finally to turn to the right when looking downslope (Figs. 3 and 5, right).
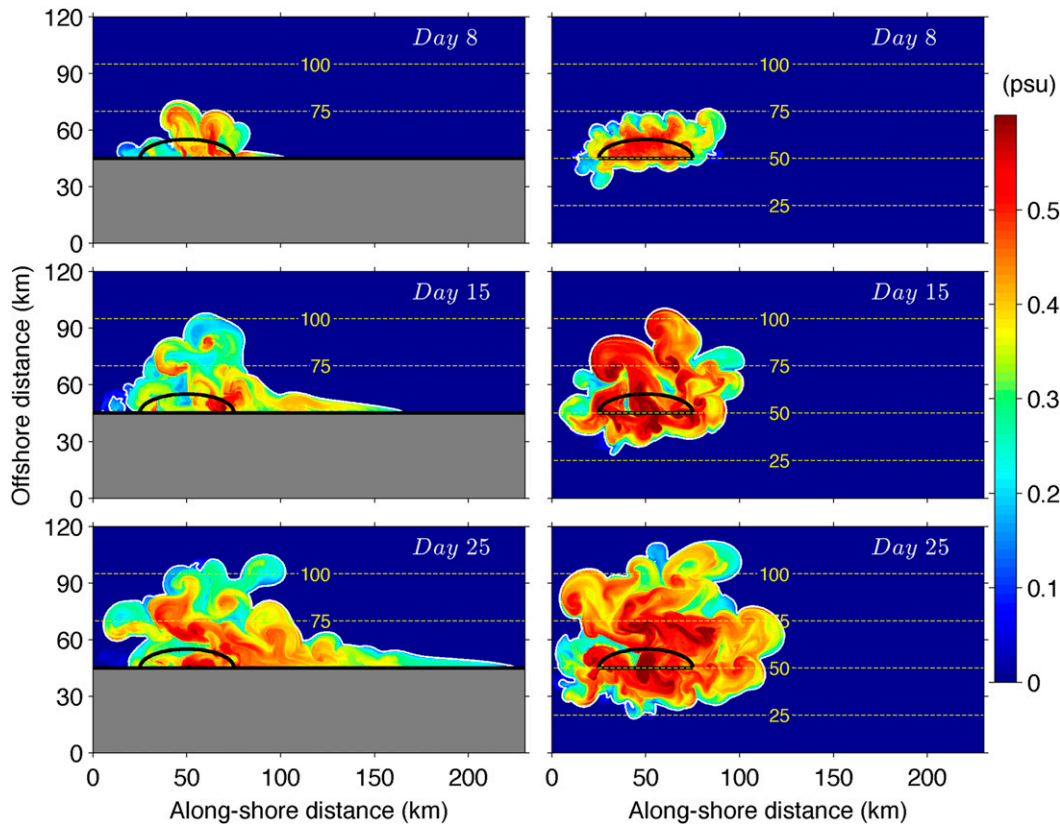
FIG. 5. Modeled bottom salinity anomaly for a polynya (left) next to and (right) away from the southern wall at days (top) 8 (inertial period 14), (middle) 15 (inertial period 26), and (bottom) 25 (inertial period 44). Black solid lines outline the polynya-forcing area; dashed yellow lines are isobath contours; white solid lines are the salinity anomaly contour of 0.2 psu.

Close examination of the model results reveals the following picture of the initial evolution of the flow structure around the perimeter of the forcing area: the near-bottom horizontal density gradient generates an anticyclonic flow presumably through the thermal wind balance; the flow develops meanders that then pinch off forming eddies that transport dense water offshore across isobaths (Fig. 2). At the eastern end of the forcing region, the bottom anticyclonic flow hits the wall, accumulating dense water there, and the increased along-shelf baroclinic pressure gradient drives the bottom coastal current. The Froude number of the bottom coastal current is defined as

$$\mathrm{Fr}_c = \frac{|\mathbf{u}_c|}{\sqrt{g'h_c}}, \qquad (5)$$

where $|\mathbf{u}_c|$ is the speed of the bottom coastal current. In the numerical control simulation, $|\mathbf{u}_c| \approx 0.05\,\mathrm{m\,s^{-1}}$ (Fig. 2), $g' \approx 0.01\,\mathrm{m\,s^{-2}}$, and $h_c = 15\,\mathrm{m}$, giving a value of $\mathrm{Fr}_c \approx 0.13$, while in the laboratory control simulation

$|\mathbf{u}_c| \approx 0.004\,\mathrm{m\,s^{-1}}$, $g' \approx 0.01\,\mathrm{m\,s^{-2}}$, and $h_c = 0.025\,\mathrm{m}$, giving a value of $\mathrm{Fr}_c \approx 0.25$.

b. Scaling of the velocities

To provide scalings for the velocities of the offshore plume and bottom coastal current, we neglect the interaction between the two transport pathways and assume that both currents reach quasi steady states or states in which flow acceleration is negligible compared to the dominant terms in the momentum balances.

For the offshore plume, we take an integrated approach, considering the motion of the whole plume instead of the motions of the individual eddies that are internal to the plume. In the vertically integrated horizontal momentum equations of the whole plume, we assume the dominant balance to be between the gravitational force F_g and the Coriolis force F_C, and all other terms, including the bottom drag and momentum advection, are neglected. The bottom drag has a minor influence as indicated by the small values of Ek_d in both the numerical and laboratory experiments (Tables 1 and 2). The advection terms are

also negligible because $\text{Ro}_d \ll 1$ indicates that they are much smaller than the Coriolis force. Thereby, we obtain the vertically integrated horizontal momentum balance:

$$fH_i|\mathbf{u}_d| \approx g'\alpha h_d, \qquad (6)$$

where H_i is the thickness of the water column that moves downslope, not only the dense layer (see below).

Equation (6) represents the steady-state limit of the offshore plume when the flow is along isobaths. During an initial "transitional" time, the descending dense water on the bottom carries the overlying column of ambient freshwater downslope crossing isobaths. Consequently, the upper layer develops positive vorticity due to vortex stretching and potential vorticity conservation, and the freshwater column above the dense layer starts spinning cyclonically (Fig. 2, right). This behavior of cross-isobath motion and the associated generation of cyclonic eddies has been observed in numerous studies (e.g., Etling et al. 2000; Lane-Serff and Baines 1998, 2000; Spall and Price 1998; Whitehead et al. 1990). After this initial transitional period the overlying eddies continue traveling with the dense current, consistent with the findings of previous laboratory and numerical studies on dense currents on sloping bottoms (Reszka et al. 2002; Sutherland et al. 2004). Hence, the Coriolis force acts not only over the thin layer of dense water near the bottom, but also over the water column above it that moves offshore with the dense water, and H_i is the thickness of the entire water column.

From (6), we obtain the average along-stream velocity of the offshore plume:

$$|\mathbf{u}_d| \approx \frac{g'\alpha}{f} \frac{h_d}{H_i}. \qquad (7)$$

Equation (7) is consistent with the long topographic Rossby wave speed on a sloping bottom with H_i being the total water depth. Equation (7) differs from the theoretical along-shelf velocity of a dense water core on a sloping bottom derived by Nof (1983), $u_g = g'\alpha/f$, by a factor of h_d/H_i. Presumably, this difference stems from the infinitely deep upper layer at rest used by Nof (1983). In our laboratory experiments, both h_d and H_i are finite, and we assume $h_d \approx h_{c0}$ and H_i to be the average ambient depth experienced by the offshore plume, while estimating the along-stream speed of the offshore plume using (7). In the numerical simulations, the slopes are gentle, $O(10^{-3})$, and a good scale for H_i is H_c, the water depth on the coast. Because the dense water in the coastal polynya initially occupies the entire water column, we assume the thickness of the offshore plume to be proportional to H_c, that is, $h_d = cH_c$, where c is

a constant. Therefore, h_d and H_i are closely related, and (7) becomes

$$|\mathbf{u}_d| \approx c\frac{g'\alpha}{f} = cu_g, \qquad (8)$$

which is used to estimate the along-stream speed of the offshore plume in the numerical experiments.

We now seek to derive a scale for the speed of the bottom coastal current $|\mathbf{u}_c|$. Although the coastal current described earlier appears similar to a two-dimensional exchange flow, the three-dimensionality of the problem and rotation make the dynamics fundamentally different. Moreover, bottom friction on the length scale of primary interest makes the analytical derivation of $|\mathbf{u}_c|$ from mass, momentum, and energy conservations, as done for gravity currents in previous studies (Hacker and Linden 2002; Linden 2012), very difficult in this case. Here, we take a momentum-balance approach and neglect the influences of coastal current cross-shelf variation, cross-shelf momentum balance, and the sloping bottom on the along-shelf momentum balance.

In a turbulent environment, Linden and Simpson (1986) showed that a lock-release gravity current can transition from an initial inviscid state to a viscous state as it proceeds in distance. Based on that finding, we separate the bottom coastal current into two stages. 1) Close to the dense water source region, viscosity effects are assumed to be small, and the steady momentum balance is between the nonlinear terms and the along-shelf baroclinic pressure gradient:

$$u \cdot \nabla u \approx -\frac{1}{\rho_0}\frac{\partial p}{\partial x}. \qquad (9)$$

Equation (9) leads to a scale for the velocity of the bottom coastal current:

$$|\mathbf{u}_c| \approx \sqrt{g'h_c}, \qquad (10)$$

which is a suitable scale for the laboratory experiments (see below). Equation (10) is essentially the speed of the interfacial gravity wave, a natural scale for velocities of Boussinesq gravity currents after their initial acceleration (Linden 2012). 2) Far away from the dense water source region, the steady momentum balance is assumed to be between the along-shelf baroclinic pressure gradient force F_P and the force exerted by the bottom stress F_D:

$$\frac{1}{\rho_0}\frac{\partial p}{\partial x} \approx \frac{1}{\rho_0}\frac{\partial \tau}{\partial z}. \qquad (11)$$

For simplicity, we assume $\partial \rho/\partial x$ to be independent of z and define L as the along-shelf span of the baroclinic
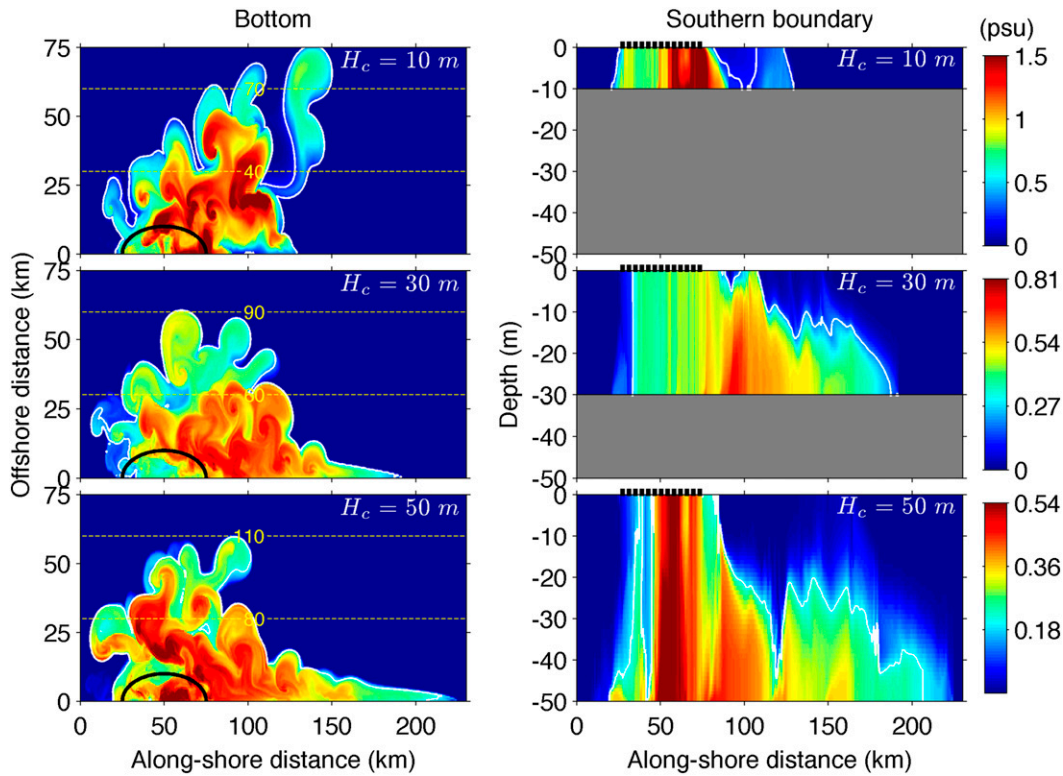
FIG. 6. Salinity anomaly (left) near the bottom and (right) along the southern wall at day 25 (inertial period 44) from simulations having different H_c. Black dashed lines in the right column indicate the polynya-forcing region; dashed yellow lines in the left column are isobath contours; white solid lines are the salinity anomaly contour of 0.2 psu.

pressure gradient. Integrating (11) over h_c and applying the quadratic bottom drag gives

$$|\mathbf{u}_c| \approx h_c \sqrt{\frac{g'}{2LC_d}}. \qquad (12)$$

Here, the near-bottom velocity is assumed to be approximately equal to $|\mathbf{u}_c|$. Equation (12) is a suitable scale for the numerical experiments (see below). In the parameter space of interest ($H_c \lesssim 50$ m), h_c is constrained by H_c, and the modeled bottom coastal current extends over the lower half of the water column (Figs. 4 and 6, right columns). Hence, we assume that the depth of the bottom coastal current is half of the depth at the coast, that is, $h_c \approx H_c/2$, as is the case for energy-conserving lock-release gravity currents (Linden 2012). The bottom coastal current velocity in the numerical setup becomes

$$|\mathbf{u}_c| \approx \frac{H_c}{2} \sqrt{\frac{g'}{2LC_d}}. \qquad (13)$$

To determine the along-shelf distance beyond which the momentum balance will be between the baroclinic

pressure gradient and the bottom stress (hereafter referred to as transitional length), we equate (10) to (12) and obtain a length scale:

$$L_c \approx \frac{h_c}{2C_d}, \qquad (14)$$

or equivalently for the laboratory setup:

$$L_c \approx \frac{\sqrt{g'h_c}\,h_c^2}{4\nu}. \qquad (15)$$

Note that the derivation of (15) is based on a relationship $C_d \approx 2\nu/(h_c|\mathbf{u}_c|)$, obtained by expressing the bottom stress both in terms of velocity shear and by a quadratic drag formula; that is, $\tau_b \approx 2\rho_0\nu|\mathbf{u}_c|/h_c \approx \rho_0 C_d|\mathbf{u}_c|^2$. Substituting $h_c = 0.025$ m, $g' \approx 0.01$ m s^{-2}, and $\nu = 10^{-6}$ m^2 s^{-1} into (15) gives $L_c \approx 2.5$ m for the laboratory experiments; substituting $h_c = 15$ m and $C_d = 0.003$ into (14) gives $L_c \approx 2.5$ km for the numerical simulations. In the laboratory experiments, the width of the tank is less than L_c. Therefore, the bottom coastal current is still in the initial inviscid stage and (10) is the appropriate scale for $|\mathbf{u}_c|$ in the laboratory. However, the associated

Froude number Fr_c (Table 2) is somewhat smaller than the Froude number observed for energy-conserving lock-release gravity currents, 0.4 (Linden 2012). Possible explanations for this discrepancy include the different methods of generating the dense gravity current and the sloping bottom in the tank. Few studies have investigated constant flux dense gravity currents, and this result calls for future investigations. In the numerical simulations, because the extent of the modeled bottom coastal current, $O(100\,\text{km})$, is much larger than L_c, the modeled bottom coastal current is in the viscous stage and bottom stress plays a dominant role, as also suggested by the small values of Fr_c (Table 1). Hence, (13) is the appropriate scale for modeled $|\mathbf{u}_c|$.

The velocity scales in (8) and (13) depend on g' and L, neither of which are external control variables in the numerical simulations. The reduced gravity depends on Q and H_c, and the numerical simulations suggest that L is related to the distance traveled by the bottom coastal current and influenced by a variety of parameters. Here, we seek to replace g' and L with external control variables of the idealized polynya system to compare the velocity scalings with results from the numerical sensitivity analysis. Based on the balance between the lateral and surface buoyancy fluxes, Chapman and Gawarkiewicz (1997) derived the equilibrium density anomaly underneath a coastal polynya:

$$\Delta\rho_e = C_c \frac{\rho_0}{gH_c}\sqrt{fQR_{Dc}b}. \tag{16}$$

Here $C_c = \sqrt{\pi/[2\gamma E(1 - b^2/a^2)]}$ is a nondimensional function of the geometry of the forcing region, $\gamma = 0.043$ is a proportionality constant, and $E(\cdot)$ is the complete elliptic integral of the second kind. Substituting the fixed values of a and b, we obtain $C_c \approx 5.63$. Note that in (16) we replace the width of the forcing decay region in the original formula in Chapman and Gawarkiewicz (1997) with the Rossby radius $R_{Dc} = (g'h_c)^{1/2}/f$. We assume $\Delta\rho_e$ to be the density anomaly of both plumes. Because $g' = g\Delta\rho_e/\rho_0$, we obtain

$$g' \approx \frac{C_c^{4/3}b^{2/3}}{2^{1/3}}\frac{Q^{2/3}}{H_c}. \tag{17}$$

The bottom coastal current forms a wedge shape with its height decreasing gradually toward the nose and its length increasing with time as the bottom coastal current flows along the wall (Figs. 4d–f). We assume that the along-shelf pressure gradient spans over the length of the wedge and, therefore, L scales with the travel distance of the bottom coastal current; that is,

$$L \approx |\mathbf{u}_c|t. \tag{18}$$

Substituting (17) and (18) into (8) and (13), we obtain

$$|\mathbf{u}_d| \approx \frac{cC_c^{4/3}b^{2/3}}{2^{1/3}}\frac{\alpha Q^{2/3}}{fH_c} \propto \frac{b^{2/3}\alpha Q^{2/3}}{fH_c} \tag{19}$$

and

$$|\mathbf{u}_c| \approx \frac{C_c^{4/9}b^{2/9}}{2^{10/9}}\frac{Q^{2/9}H_c^{1/3}}{C_d^{1/3}t^{1/3}} \propto \frac{b^{2/9}Q^{2/9}H_c^{1/3}}{C_d^{1/3}t^{1/3}}, \tag{20}$$

respectively. The ratio of $|\mathbf{u}_d|$ and $|\mathbf{u}_c|$ is therefore

$$\frac{|\mathbf{u}_d|}{|\mathbf{u}_c|} \propto \frac{b^{4/9}\alpha Q^{4/9}C_d^{1/3}t^{1/3}}{fH_c^{4/3}}. \tag{21}$$

The time-dependent scaling of $|\mathbf{u}_c|$ in (20) indicates that the momentum balance the scaling analysis is based on does not allow a steady-state coastal current. The scaled weak time dependence of $t^{-1/3}$ is the same as the time dependence in the scaled speed of a "similarity phase" gravity current resulting from a finite volume lock release (Linden 2012). By comparing the acceleration term, $\partial|\mathbf{u}_c|/\partial t$, to the viscous terms (equivalently, the pressure gradient term) in (11) and applying (17), (18), and (20), we obtain a characteristic time scale of frictional adjustment,

$$T_a = \frac{2^{1/6}H_c}{3^{3/2}C_c^{2/3}b^{1/3}Q^{1/3}C_d}, \tag{22}$$

that provides a measure of the importance of $\partial|\mathbf{u}_c|/\partial t$: when $t \gg T_a$, $\partial|\mathbf{u}_c|/\partial t$ is negligible relative to the two terms in (11). Substituting the parameters of the control simulation (Table 1) into (22) gives $T_a \approx 0.05$ day, and among all the simulations, the maximum T_a is 0.5 days (when $C_d = 0.3 \times 10^{-3}$). The analysis of the numerical experiments focuses on the period after day 25; thus, it is reasonable to neglect the acceleration of the bottom coastal current even with a time-dependent velocity scaling.

In the next two subsections, we will compare the derived velocity scalings with numerical and laboratory sensitivity experiments conducted with different values of α, Q, C_d, f, and H_c for the numerical simulations and α, $Q_V(h_c)$, f, and g' for the laboratory experiments.

c. Numerical sensitivity tests

The bottom and along-shelf salinity anomalies at day 25 (inertial period 44) from simulations with different depths on the coast, H_c, (Fig. 6) show that within the same time period the distance the offshore plume travels decreases with increasing H_c, especially for H_c increasing from 10 to 30 m, and the distance the bottom coastal
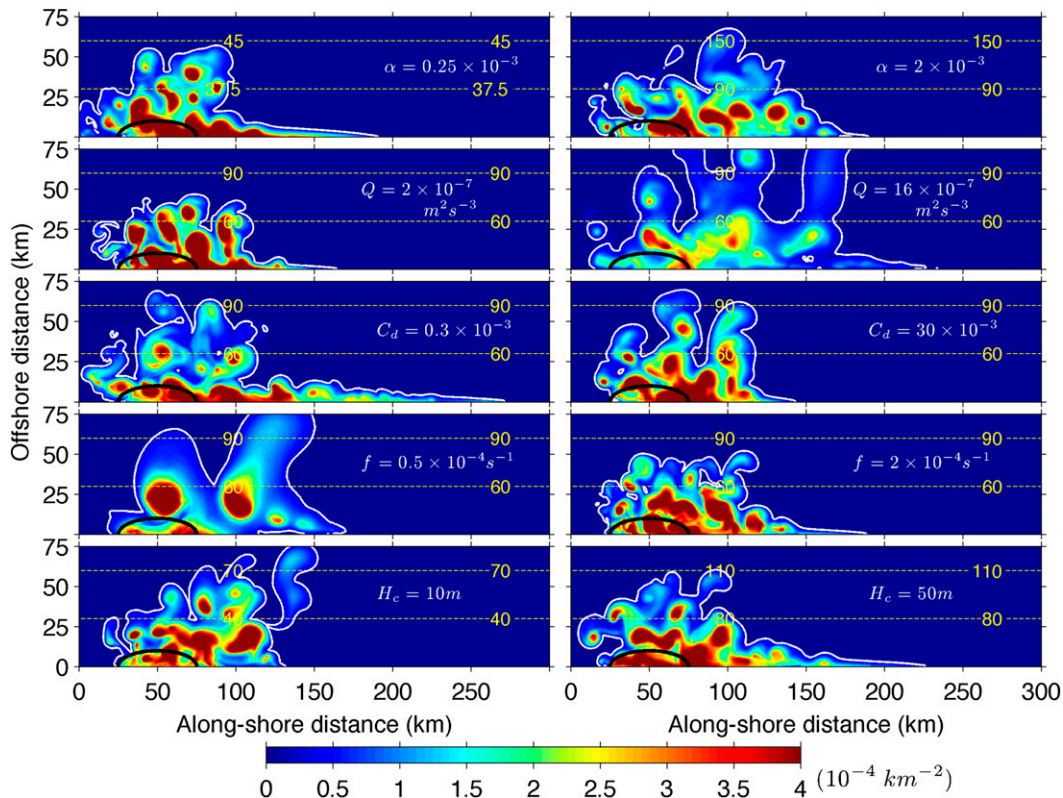
FIG. 7. Vertically integrated salinity anomaly at day 25 (inertial period 17 and 68 for left and right in the fourth row, respectively, and 44 for all others) normalized by the total salinity anomaly in the domain. Black solid lines indicate the polynya region; dashed yellow lines are isobath contours; white solid lines are the contour of $0.2 \times 10^{-4} \, km^{-2}$ normalized salinity anomaly.

current travels increases dramatically with increasing H_c. These results suggest that H_c exerts a profound influence on velocities of both the offshore plume and the bottom coastal current.

To illustrate the effect of all the control parameters on dense water dispersal, the vertically integrated normalized salinity anomaly at day 25 from two selected sensitivity simulations of each series are shown in Fig. 7. The distance the offshore plume travels in 25 days increases with increasing α and Q and decreases with increasing f and H_c; the distance the bottom coastal current travels increases with increasing Q and H_c and decreases with increasing C_d. This dependence on C_d confirms that the modeled bottom coastal current is in the viscous stage and its velocity should scale with (13). For a more quantitative comparison of the parameter dependences, in the numerical solutions we compute $|\mathbf{u}_c|$ and $|\mathbf{u}_d|$ from the distances the heads of the dense water plumes travel away from the polynya region in the first 25 days. The general pattern of the modeled velocities versus the control parameters in Fig. 8 is consistent with the scaled relationships in (19) and (20). Moreover, $|\mathbf{u}_d|$

is not dependent on C_d, and $|\mathbf{u}_c|$ is not dependent on f. Figure 8f shows a weak dependence of $|\mathbf{u}_c|$ on α, with $|\mathbf{u}_c|$ decreasing for increasing α. We will discuss this dependence below.

In Fig. 9, modeled $|\mathbf{u}_d|$, $|\mathbf{u}_c|$ and $|\mathbf{u}_d|/|\mathbf{u}_c|$ are compared to the scalings in (19), (20), and (21) of the corresponding simulations, respectively. The constant factor c in the scalings is neglected. The results fall around straight lines in all comparisons, suggesting that, in the parameter space we have investigated, the scaling analyses are largely consistent with the numerically modeled dynamics. Slight differences in the comparisons, including a small amount of scatter and the nonzero intercepts, are presumably caused by the assumptions or missing dynamics in the scaling analyses.

Although the numerical simulations agree with the scaled relationships between the velocities and the control parameters, the reduction of $|\mathbf{u}_c|$ when α increases (Fig. 8f) is unexplained. Possible causes include the interactions between the two pathways and the cross-shelf momentum balance in the bottom coastal current. In particular, when α increases, more dense water moves
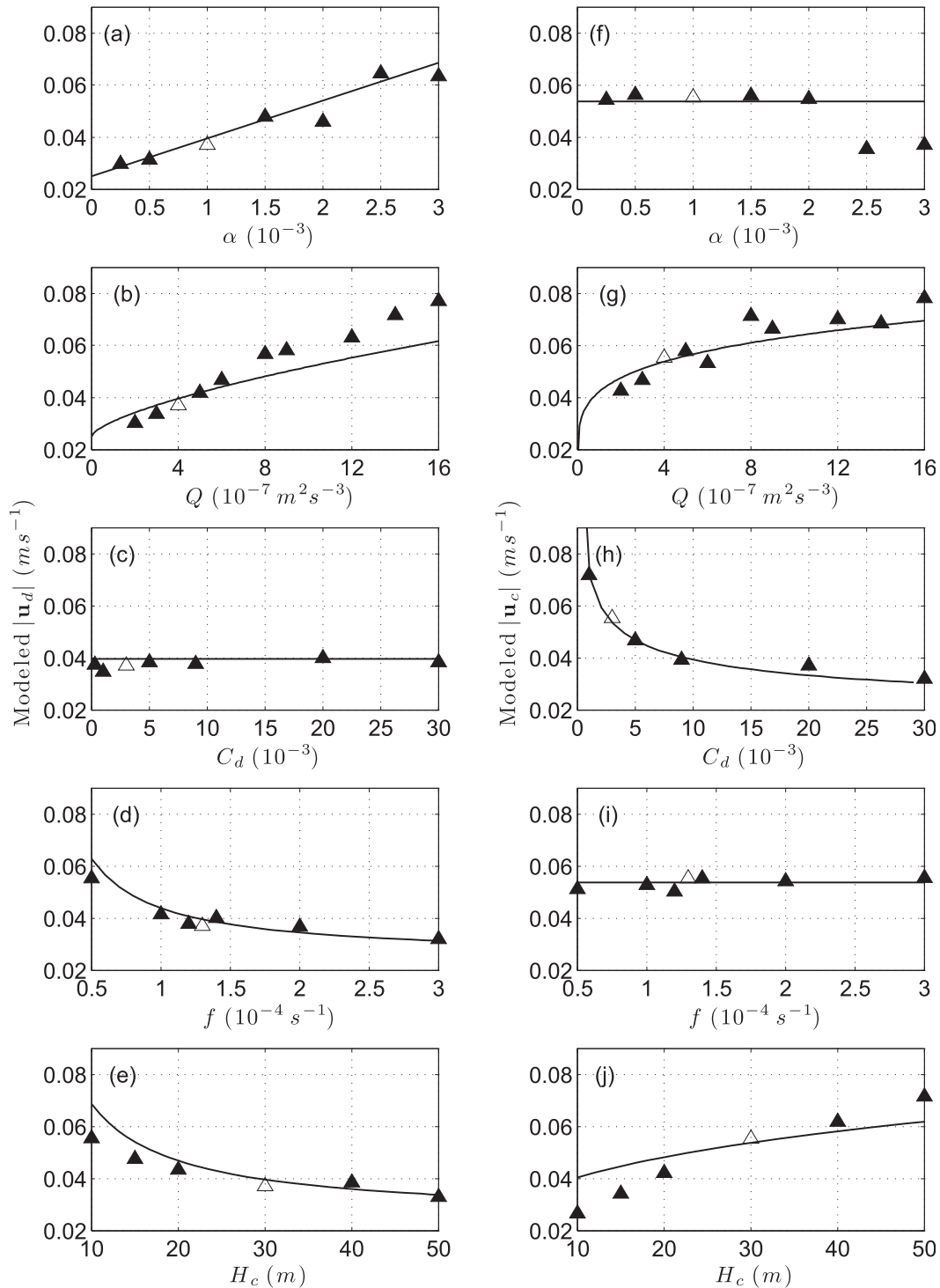
FIG. 8. Variation of modeled (left) $|\mathbf{u}_d|$ and (right) $|\mathbf{u}_c|$ with respect to different parameters. The open symbols represent the control simulation. The black lines represent the relationships of $|\mathbf{u}_d|$ and $|\mathbf{u}_c|$ with each parameter as described by (19) and (20) and with the coefficients obtained from least squares fits to all the modeled vs scaled velocities (the black lines in Figs. 9a and 9b).
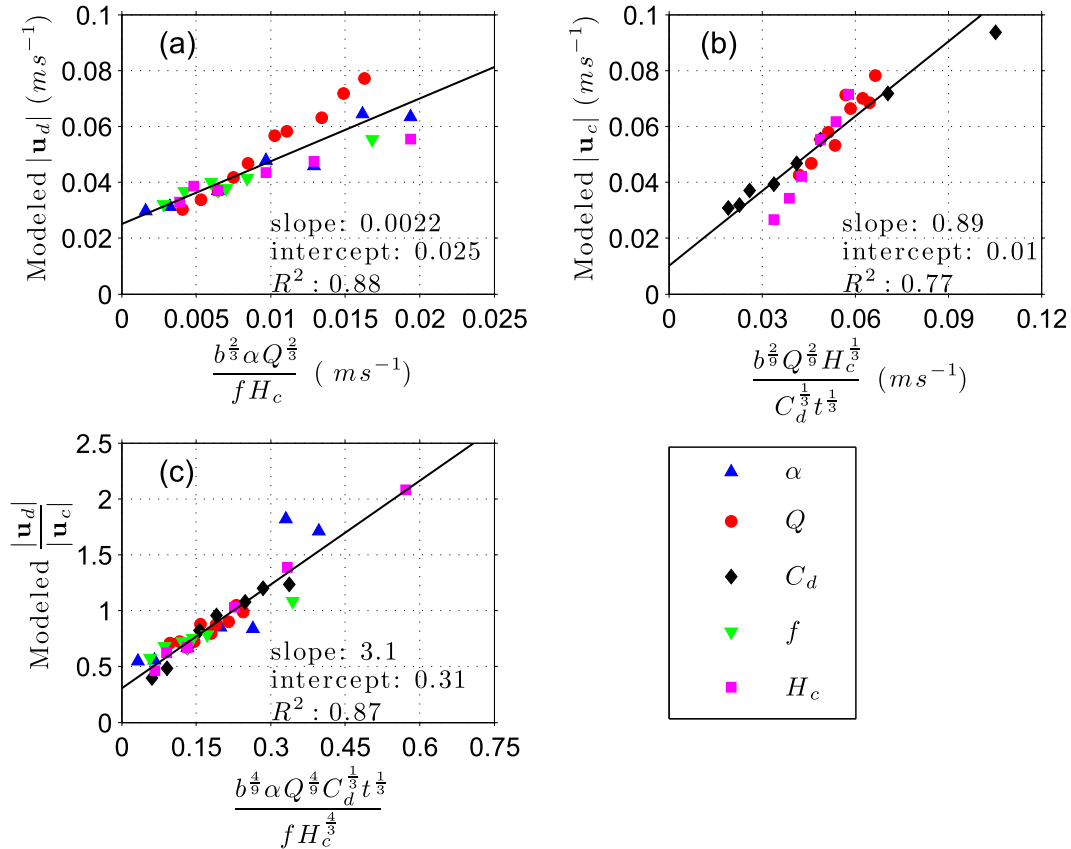
FIG. 9. Modeled (a) $|\mathbf{u}_d|$, (b) $|\mathbf{u}_c|$, and (c) $|\mathbf{u}_d|/|\mathbf{u}_c|$ vs scalings in (19), (20), and (21), respectively. Note that each type of symbol represents comparisons obtained through varying one parameter as shown in the legend. Solid lines are least squares fits to all points; the slope, intercept, and R^2 of the fits are given.

offshore and less water accumulates at the eastern end of the polynya forcing region, reducing the amount of dense water available for generating the bottom coastal current. In addition, the downslope component of gravity may force some of the dense water already in the bottom coastal current to move offshore, generating the dense water eddies near the tail of the bottom coastal current (Fig. 7, top-right). These dynamics are neglected in the scaling analysis, but capable of reducing the strength of the along-shelf pressure gradient and consequently the velocity of the bottom coastal current.

Finally, the numerical simulations do not resolve nonhydrostatic processes in the system, including convection within the polynya, strong vertical motions at the noses of the dense currents, and Kelvin–Helmholtz instabilities at the interface between the dense and ambient waters. As the nonhydrostatic processes generally take place on the scale of tens of meters, our model with a horizontal resolution of 500 m is not capable of resolving them, and the associated mixing can only be included through turbulence parameterization. Because this study focuses on the transport of dense

water occurring over horizontal scales of tens of kilometers, we believe that the nonhydrostatic processes do not influence the momentum balance at first order or fundamentally change the results. However, it is possible that the parameterized entrainment of ambient water into the plume is inadequate and may affect details of the plumes.

d. Laboratory sensitivity tests

Figures 10 and 11 show the dependence of the time-averaged velocities, $|\mathbf{u}_d|$ and $|\mathbf{u}_c|$, on the control parameters varied in the laboratory. The velocities are calculated from the distances that the heads of the dense water plumes travel in the time it takes the bottom coastal current to first reach the downstream edge of the tank. The bottom coastal current forms a wedge shape, as observed in the numerical simulations, and we assume $h_c = h_{c0}/2$. The patterns in Fig. 10 are generally consistent with the parameter dependence described in (7) and (10); $|\mathbf{u}_d|$ increases with α, h_c, and g' and $|\mathbf{u}_c|$ increases with h_c and g'. Note that in the laboratory experiments h_c is not a control variable, but it varies with the control
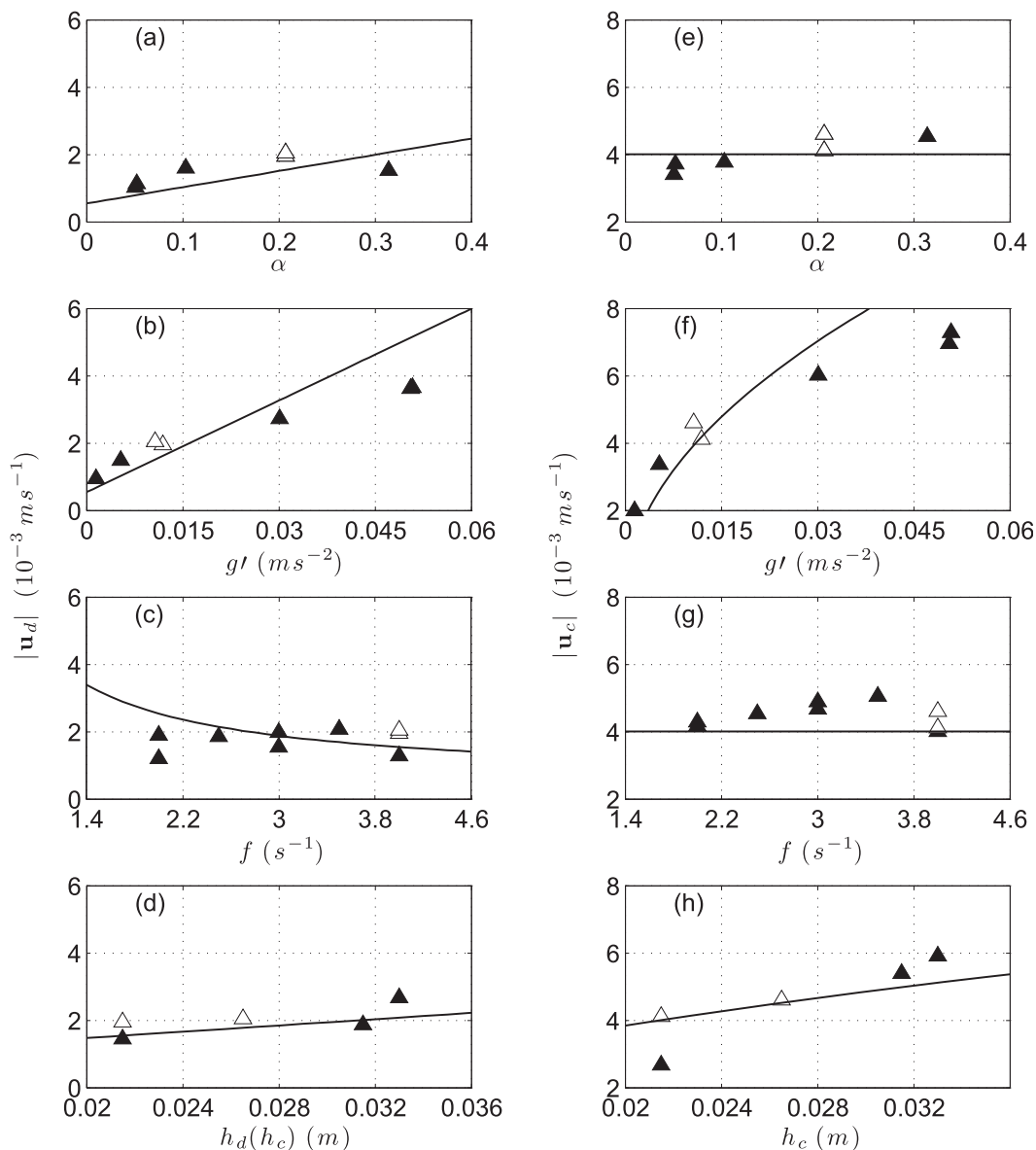
FIG. 10. Variation of measured (left) $|\mathbf{u}_d|$ and (right) $|\mathbf{u}_c|$ with respect to different parameters varied in the laboratory experiments. Open symbols represent the control experiment. The black lines represent the relationships of $|\mathbf{u}_d|$ and $|\mathbf{u}_c|$ with each parameters as described by (7) and (10) and with the coefficients obtained from least squares fits to all the measured vs scaled velocities (the black lines in Fig. 11).

variables, including g'. This deteriorates the comparisons of the scaled and computed trends in Figs. 10b and 10f, and the actual trend comparisons are better when both h_c and g' are considered (Fig. 11). We find no dependence of $|\mathbf{u}_d|$ on f (Fig. 10c) as (7) would suggest. Furthermore, Figs. 10e and 10g show a weak dependence of $|\mathbf{u}_c|$ on α and f with $|\mathbf{u}_c|$ increasing when α and f increase, which is not described in (10). Figure 11 shows that the measured $|\mathbf{u}_d|$ and $|\mathbf{u}_c|$ are consistent with the scalings proposed in (7) and (10), albeit the results present some scatter around the least squares fit of the

data. Overall, the laboratory results largely confirm the findings of the numerical experiments and the validity of the scaling analyses in the parameter space that we have tested.

The exact cause of the lack of dependence of $|\mathbf{u}_d|$ on f remains unclear. One possible reason is that, in the laboratory, the Rossby number Ro_d (equivalent to Fr_d in this study) is much smaller than in the numerical simulations (Tables 1 and 2), and the numerical simulations indicate that the dependence of $|\mathbf{u}_d|$ with respect to f decreases with increasing f (Fig. 7d). Thus, it is possible
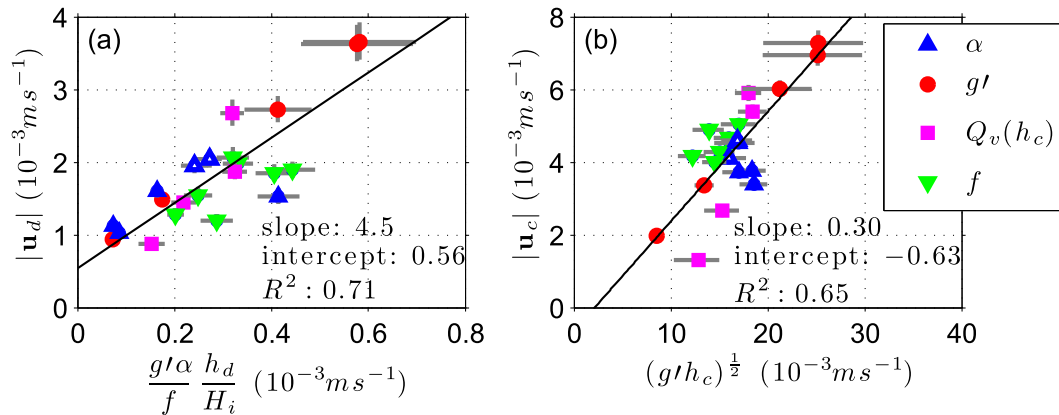
FIG. 11. (a) $|\mathbf{u}_d|$ and (b) $|\mathbf{u}_c|$ measured in the laboratory vs scalings in (7) and (10), respectively. Each type of symbol represents comparisons obtained through varying one parameter as shown in the legend. Open symbols represent the control experiments; gray lines are estimated error bars; solid lines are least squares fits to all points, and the slope, intercept, and R^2 of the fits are given.

that f in the laboratory is too large to influence $|\mathbf{u}_d|$. Furthermore, it is worth noticing that in the laboratory h_c (equivalently, h_{c0}) is not an external control parameter and slightly varies with varying target parameters, including α and f. This may cause the weak dependence of $|\mathbf{u}_c|$ on α and f (Figs. 10e,g).

e. Volume transport of the salinity anomaly

Results of the numerical simulations are used to investigate the fate of the dense water formed in a coastal polynya on a shallow sloping shelf. To avoid the ambiguity associated with dense water exchange between the two pathways, we choose to compute the volume-integrated salinity anomaly in the offshore plume and bottom coastal current at day 40 (Fig. 12) and use their ratio to represent the relative amount of dense water in the two pathways. The bottom coastal current is defined as the region within 12 km offshore from the coast east of the polynya, while all salinity anomalies outside of the 12-km-wide coastal band region and also outside of the polynya-forcing region are considered to be in the off-shore pathway.

As observed for the velocity ratio, the fraction of salinity anomaly in the bottom coastal current [$V_c/(V_c + V_d)$, where V_c and V_d are the amount of salinity anomaly in the bottom coastal current and offshore plume, respectively] varies with the parameters investigated in the numerical sensitivity analysis. In general, there is a tendency for $V_c/(V_c+V_d)$ to decrease with increasing α, Q, and C_d and increase with increasing f and H_c (Fig. 12). Overall, about 3%–23% of the dense water generated in the coastal polynya flows in the bottom coastal current, and this percentage correlates inversely with the velocity ratio in (21) (Fig. 13a).

Even though only a relatively small fraction of the dense water moves along the coast, it is important to recognize the existence of the dense water bottom coastal current generated by the polynya processes. The predicted percentage may also be helpful for indirectly estimating from observations the total amount of dense water formed by a particular polynya event or the total off-shore dense water transport. Figure 13b illustrates the clear dependence of the ratio of the offshore and coastal dense waters transport (V_d/V_c) to the ratio of the plume velocities. Presumably, the transport in the narrow bottom coastal current can be measured more easily and reliably than the transport in the broad offshore dense water plume. Therefore, given the ratio of the velocity scalings and the empirical relationships in Fig. 13b, in situ measurements of V_c could be used to assess the amount of dense water in the offshore plume, V_d. Of course, because of the uncertainties embedded in the empirical relationship between V_d/V_c and $|\mathbf{u}_d|/|\mathbf{u}_c|$, any percentage error in the in situ V_c measurements would be magnified in the V_d estimate, and the absolute error range would be even larger since $V_d \gg V_c$. For instance, for the scenario of $V_d/V_c \approx 10$, a 10% uncertainty in the V_c measurement would lead to an uncertainty of about 39% in the V_d estimate if the empirical relationship obtained from the quadratic fit (Fig. 13b) is used with the assumed error bar of one rms error (RMSE).

4. Summary

This study combines analytical scaling analyses, numerical simulations, and laboratory experiments to investigate the dispersal and fate of dense water formed in a coastal polynya on a shallow continental shelf in the
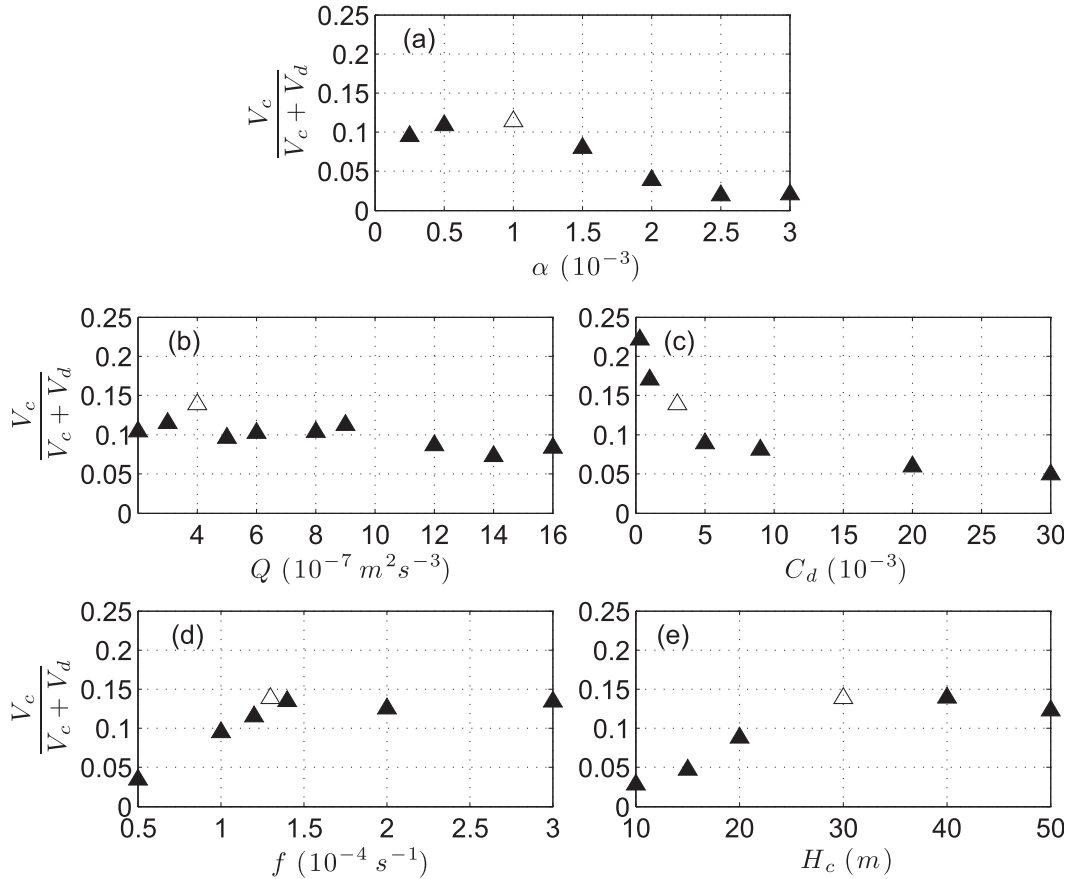
FIG. 12. Variation of the fraction of salinity anomaly in the coastal current $[V_c/(V_c + V_d)]$ at day 40 with respect to different parameters. The open symbols represent the control simulation.

absence of ambient circulation, ambient stratification, and surface stress forcing. Overall, the results of the different methodologies largely agree with each other, suggesting that the fundamental physics of the dense water dispersal processes are captured by the scaling analyses.

Both numerical and laboratory experiments show two separate pathways for the bottom dispersal of the dense water: a fraction of the dense water moves initially offshore down the slope and then turns right (looking downslope), while another fraction flows along the coast in the direction of Kelvin wave propagation. The formation of this latter transport pathway in a coastal polynya environment has been seldom studied, and its dynamics and significance are overlooked in the literature.

Scaling analysis based on the momentum balance in the offshore dense water pathway shows that the velocity of the offshore plume is proportional not only to $g'\alpha/f$, the characteristic speed of a dense water current on a sloping bottom derived by previous studies of dense water overflows, but also to the ratio of the dense water depth to total water depth, h_d/H_i. The laboratory

sensitivity experiments confirm this relationship (Figs. 10 and 11). In the numerical setup, since the bottom slope is very gentle as on most of the continental shelves in the Arctic Ocean, H_i in the scaling can be replaced by the water depth at the coast H_c. Because the dense water initially occupies the entire water column, we assume the thickness of the offshore plume, h_d, to be proportional to H_c. Hence, the velocity depends solely on $g'\alpha/f$, which translates to a scale of $b^{2/3}\alpha Q^{2/3}/(fH_c)$ using the external control parameters of the polynya. This relationship agrees with results of the numerical sensitivity experiments (Figs. 8 and 9).

The dense water bottom coastal current is generated by the baroclinic pressure gradient along the coastal wall and can be described by two dynamical stages separated by the transitional length scale: $L_c \approx h_c/(2C_d) = \sqrt{g'h_c}h_c^2/(4\nu)$. Before the current reaches the distance L_c (in the near field of the source region), the viscous terms are small and the nonlinear advection terms balance the pressure gradient force. The speed of the bottom coastal current in this stage is proportional to the reduced gravity wave speed $\sqrt{g'h_c}$. Limited by the size of the tank, bottom
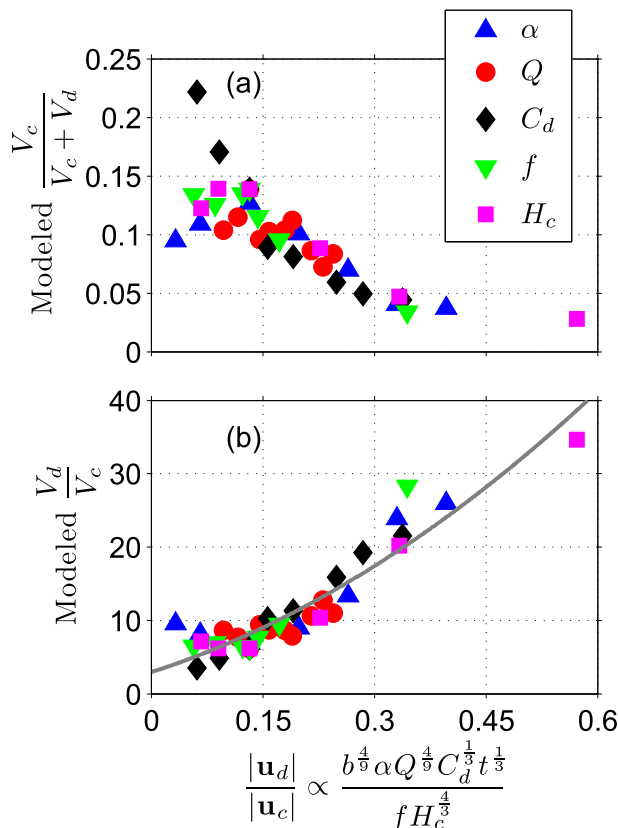
FIG. 13. A comparison of (a) the fraction of salinity anomaly in the coastal current and (b) the ratio of the amount of salinity anomaly in the two pathways at day 40 with the velocity ratio in (21). The gray line in (b) represents the fit given by $y = 52.1x^2 + 32.6x + 2.9$ with $R^2 = 0.88$ and RMSE = 2.6.

from in situ measurements of the relatively narrow bottom coastal current. Of course, considerable uncertainties will be associated with this type of estimate because of the large ratio of the offshore to coastal transports and uncertainties in the empirical relationship between transport and velocity ratios and also in the measurements. Moreover, a number of factors, for example, winds, irregular topography, ambient current, ambient stratification, and the vertical shape of the ice edge (floating land-fasted ice instead of grounding ice edge), which are all neglected in this study, can influence the dynamics and the relationship between the transport and velocity ratio. To what extent these factors will change the scaled relationships remains to be studied.

coastal currents in the laboratory experiments all fall into this category, and the sensitivity experiments confirm the velocity scaling. In the far field, after the current passes L_c, bottom drag becomes the dominant force to balance the pressure gradient, and the speed is proportional to $b^{2/9}Q^{2/9}H_c^{1/3}/(C_d^{1/3}t^{1/3})$. The numerically modeled bottom coastal currents reflect this second stage dynamics, and the results of the sensitivity simulations verify the velocity scaling. As expected, some details in the scaling, numerical, and laboratory results are different, which could be caused by a number of factors, including the assumptions made in the scaling analyses and the different methods of supplying the dense water in the numerical and laboratory experiments.

The numerical simulations also suggest that the dense water transport in the coastal pathway is relatively low, 3%–23% of the total transport, and that the percentage depends strongly on the ratio of the offshore and coastal plume velocities given by (21) (Fig. 13). Therefore, the velocity ratio could be used to indirectly estimate the total amount of dense water formed in a coastal polynya

REFERENCES

Aagaard, K., L. K. Coachman, and E. Carmack, 1981: On the halocline of the Arctic Ocean. *Deep-Sea Res. I,* **28,** 529–545, doi:10.1016/0198-0149(81)90115-1.

Cavalieri, D. J., and S. Martin, 1994: The contribution of Alaskan, Siberian, and Canadian coastal polynyas to the cold halocline layer of the Arctic Ocean. *J. Geophys. Res.,* **99,** 18 343–18 362, doi:10.1029/94JC01169.

Cenedese, C., and C. Adduce, 2008: Mixing in a density-driven current flowing down a slope in a rotating fluid. *J. Fluid Mech.,* **604,** 369–388, doi:10.1017/S0022112008001237.

——, J. A. Whitehead, T. A. Ascarelli, and M. Ohiwa, 2004: A dense current flowing down a sloping bottom in a rotating fluid. *J. Phys. Oceanogr.,* **34,** 188–203, doi:10.1175/1520-0485(2004)034<0188:ADCFDA>2.0.CO;2.

Chapman, D. C., 1985: Numerical treatment of cross-shelf open boundaries in a barotropic ocean model. *J. Phys. Oceanogr.,* **15,** 1060–1075, doi:10.1175/1520-0485(1985)015<1060:NTOCSO>2.0.CO;2.

——, 1999: Dense water formation beneath a time-dependent coastal polynya. *J. Phys. Oceanogr.,* **29,** 807–820, doi:10.1175/1520-0485(1999)029<0807:DWFBAT>2.0.CO;2.

——, 2000: The influence of an alongshelf current on the formation and offshore transport of dense water from a coastal polynya. *J. Geophys. Res.,* **105,** 24 007–24 019, doi:10.1029/2000JC000296.

——, and G. Gawarkiewicz, 1995: Offshore transport of dense shelf water in the presence of a submarine canyon. *J. Geophys. Res.,* **100,** 13 373–13 387, doi:10.1029/95JC00890.

——, and ——, 1997: Shallow convection and buoyancy equilibration in an idealized coastal polynya. *J. Phys. Oceanogr.,* **27,** 555–566, doi:10.1175/1520-0485(1997)027<0555:SCABEI>2.0.CO;2.

Chen, S.-N., W. R. Geyer, and T.-J. Hsu, 2013: A numerical investigation of the dynamics and structure of hyperpycnal river plumes on sloping continental shelves. *J. Geophys. Res.,* **118,** 2702–2718, doi:10.1002/jgrc.20209.

Etling, D., F. Gelhardt, U. Schrader, F. Brennecke, G. Kuhn, G. C. d'Hieres, and H. Didelle, 2000: Experiments with density currents on a sloping bottom in a rotating fluid. *Dyn. Atmos. Oceans,* **31,** 139–164, doi:10.1016/S0377-0265(99)00031-7.

Flather, R. A., 1976: A tidal model of the northwest European continental shelf. *Mem. Soc. Roy. Sci. Liege,* **10,** 141–164.

Gawarkiewicz, G., 2000: Effects of ambient stratification and shelfbreak topography on offshore transport of dense water on continental shelves. *J. Geophys. Res.,* **105,** 3307–3324, doi:10.1029/1999JC900298.

——, and D. C. Chapman, 1995: A numerical study of dense water formation and transport on a shallow, sloping continental shelf. *J. Geophys. Res.,* **100,** 4489–4507, doi:10.1029/94JC01742.

Griffiths, R. W., and E. J. Hopfinger, 1983: Gravity currents moving along a lateral boundary in a rotating fluid. *J. Fluid Mech.,* **134,** 357–399, doi:10.1017/S0022112083003407.

Hacker, J. N., and P. F. Linden, 2002: Gravity currents in rotating channels. Part 1. Steady-state theory. *J. Fluid Mech.,* **457,** 295–324, doi:10.1017/S0022112001007662.

Haidvogel, D. B., and Coauthors, 2008: Ocean forecasting in terrain-following coordinates: Formulation and skill assessment of the regional ocean modeling system. *J. Comput. Phys.,* **227,** 3595–3624, doi:10.1016/j.jcp.2007.06.016.

Jiang, L., and W. Garwood Jr., 1996: Three-dimensional simulations of overflows on continental slopes. *J. Phys. Oceanogr.,* **26,** 1224–1233, doi:10.1175/1520-0485(1996)026<1214: TDSOOO>2.0.CO;2.

Killworth, P. D., and N. R. Edwards, 1999: A turbulent bottom boundary layer code for use in numerical ocean models. *J. Phys. Oceanogr.,* **29,** 1221–1238, doi:10.1175/1520-0485(1999)029<1221: ATBBLC>2.0.CO;2.

Lane-Serff, G. F., and P. G. Baines, 1998: Eddy formation by dense flows on slopes in a rotating fluid. *J. Fluid Mech.,* **363,** 229–252, doi:10.1017/S0022112098001013.

——, and ——, 2000: Eddy formation by overflows in stratified water. *J. Phys. Oceanogr.,* **30,** 327–337, doi:10.1175/ 1520-0485(2000)030<0327:EFBOIS>2.0.CO;2.

Lentz, S. J., and K. R. Helfrich, 2002: Buoyant gravity currents along a sloping bottom in a rotating fluid. *J. Fluid Mech.,* **464,** 251–278, doi:10.1017/S0022112002008868.

Linden, P., 2012: Gravity current—Theory and laboratory experiments. *Buoyancy-Driven Flows,* E. P. Chassignet, C. Cenedese, and J. Verron, Eds., Cambridge University Press, 13–51.

——, and J. E. Simpson, 1986: Gravity-driven flows in a turbulent fluid. *J. Fluid Mech.,* **172,** 481–497, doi:10.1017/ S0022112086001829.

Mahoney, A., H. Eicken, A. G. Gaylord, and L. Shapiro, 2007: Alaska landfast sea ice: Links with bathymetry and atmospheric circulation. *J. Geophys. Res.,* **112,** C02001, doi:10.1029/ 2006JC003559.

Morales Maqueda, M. A., A. J. Willmott, and N. R. T. Biggs, 2004: Polynya dynamics: A review of observations and modeling. *Rev. Geophys.,* **42,** RG1004, doi:10.1029/2002RG000116.

Nof, D., 1983: The translation of isolated cold eddies on a sloping bottom. *Deep-Sea Res.,* **30,** 171–182, doi:10.1016/ 0198-0149(83)90067-5.

Orlanski, I., 1976: A simple boundary condition for unbounded hyperbolic flows. *J. Comput. Phys.,* **21,** 251–269, doi:10.1016/ 0021-9991(76)90023-1.

Price, J. F., and M. O. Baringer, 1994: Outflows and deep water production by marginal seas. *Prog. Oceanogr.,* **33,** 161–200, doi:10.1016/0079-6611(94)90027-2.

Reszka, M. K., G. E. Swaters, and B. R. Sutherland, 2002: Instability of abyssal currents in a continuously stratified ocean with bottom topography. *J. Phys. Oceanogr.,* **32,** 3528–3550, doi:10.1175/1520-0485(2002)032<3528:IOACIA>2.0.CO;2.

Shchepetkin, A. F., and J. C. McWilliams, 2008: Computational kernel algorithms for fine-scale, multiprocess, long-term oceanic simulations. *Computational Methods for the Atmosphere and the Ocean,* P. G. Ciarlet, R. Temam, and J. Tribbia, Eds., Vol. 14, *Handbook of Numerical Analysis,* Elsevier, 121–183.

Spall, M. A., and J. F. Price, 1998: Mesoscale variability in Denmark Strait: The PV outflow hypothesis. *J. Phys. Oceanogr.,* **28,** 1598–1623, doi:10.1175/1520-0485(1998)028<1598: MVIDST>2.0.CO;2.

Stern, M. E., J. A. Whitehead, and B.-L. Hua, 1982: The intrusion of a density current along the coast of a rotating fluid. *J. Fluid Mech.,* **123,** 237–265, doi:10.1017/S0022112082003048.

Sutherland, B. R., J. Nault, K. Yewchuk, and G. E. Swaters, 2004: Rotating dense currents on a slope. Part 1. Stability. *J. Fluid Mech.,* **508,** 241–264, doi:10.1017/S0022112004009176.

Warner, J. C., C. R. Sherwood, H. G. Arango, and R. P. Signell, 2005: Performance of four turbulence closure models implemented using a generic length scale method. *Ocean Modell.,* **8,** 81–113, doi:10.1016/j.ocemod.2003.12.003.

Whitehead, J. A., M. Stern, G. R. Flierl, and B. Klinger, 1990: Experimental observations of baroclinic eddies on a sloping bottom. *J. Geophys. Res.,* **95,** 9585–9610, doi:10.1029/ JC095iC06p09585.

Wilchinsky, A. V., and D. L. Feltham, 2008: Generation of a buoyancy-driven coastal current by an Antarctic polynya. *J. Phys. Oceanogr.,* **38,** 1011–1032, doi:10.1175/2007JPO3831.1.

Winsor, P., and G. Björk, 2000: Polynya activity in the Arctic Ocean from 1958 to 1997. *J. Geophys. Res.,* **105,** 8789–8803, doi:10.1029/1999JC900305.

——, and D. C. Chapman, 2002: Distribution and interannual variability of dense water production from coastal polynyas on the Chukchi Shelf. *J. Geophys. Res.,* **107,** 3079, doi:10.1029/ 2001JC000984.

Wobus, F., G. I. Shapiro, M. A. M. Maqueda, and J. M. Huthnance, 2011: Numerical simulations of dense water cascading on a steep slope. *J. Mar. Res.,* **69,** 391–415, doi:10.1357/ 002224011798765268.

Yankovsky, A. E., and D. C. Chapman, 1997: A simple theory for the fate of buoyant coastal discharges. *J. Phys. Oceanogr.,* **27,** 1386–1401, doi:10.1175/1520-0485(1997)027<1386: ASTFTF>2.0.CO;2.

Zilitinkevich, S., and D. V. Mironov, 1996: A multi-limit formulation for the equilibrium depth of a stably stratified boundary layer. *Bound.-Layer Meteor.,* **81,** 325–351, doi:10.1007/BF02430334.